Submerged Vortex Morphology and Pressure Fluctuation Characteristics in Intake Sump

X. Hou[1], J. Yuan[1†], Y. Fu[2], P. Wang[1], P. Zhang[1] and N. He[1]

[1] Research Center of Fluid Machinery Engineering and Technology, Jiangsu University, Zhenjiang 212013, China
[2] School of Energy and Power Engineering, Jiangsu University, Zhenjiang 212013, China

†Corresponding Author Email: 2212111015@stmail.ujs.edu.cn

ABSTRACT

This study investigates the characteristics of submerged vortices in an intake sump through a combination of numerical simulations, experimental validations, and advanced modeling techniques. The aim of this study is to gain insights into the complex flow patterns and vortex structures within the sump, focusing on their behavior under varying flow rates. The Shear Stress Transfer (SST) k-ω model is utilized to capture turbulence, and the Volume of Fluid (VOF) method is employed to visualize the water-air interface. Model tests are conducted to validate the simulations. The findings suggest that under low flow conditions, the flow beneath the bell mouth becomes highly turbulent, leading to the formation of a complex vortex system with three distinct high-pressure zones. With increasing flow rates, the shape and strength of these high-pressure zones fluctuate, and a quadrupole vortex structure emerges at the sump bottom. This quadrupole vortex plays a pivotal role in the transformation of a floor-attached vortex upward, culminating in a dual vortex column structure. This structure, in turn, generates additional low-amplitude pressure pulsations. Wall-attached vortices are also observed on both sides of the inlet pipe, a result of flow stratification due to velocity disparities. The insights gained from this study contribute to a deeper understanding of intake sump dynamics and offer valuable guidance for designing and optimizing fluid systems to mitigate potential turbulence-related issues.

1. INTRODUCTION

Vortices, abundant in engineering applications, particularly in hydraulic structures, are persistent phenomena in fluid dynamics that have detrimental effects on pumping stations. The ocean, as an open natural intake sump, represents a significant challenge for offshore engineering platforms, such as marine pumping stations. During the water intake process, the occurrence of both free-surface and submerged vortices is highly probable. Submerged vortices, primarily composed of floor-attached, sidewall-attached, and rear-wall-attached vortices, frequently occur beneath the liquid surface (Rajendran, 1998). Despite numerous renovations and upgrades to many pumping stations, which include adopting top-sealed lateral intake structures to mitigate the impact of free-surface vortices, the presence of submerged vortices remains an unavoidable issue. The occurrence of submerged vortices leads to a significant reduction in water pressure near the vortex core, causing gases to be released from the water. Should the accumulation of gas reach a critical level, the gas-laden vortices may enter the pump apparatus, leading to wear and vibration, impairing its proper function, and potentially causing substantial losses (Song & Liu, 2020). Consequently, it is essential to investigate the generation and evolution mechanisms of submerged vortices to reduce their occurrence and enhance the performance of engineering applications.

With the ongoing advancement of pumping station technology, scholars both domestically and internationally have been delving deeper into vortex research. Initially, researchers (Wu, 1985; Huang & Hu, 2000; Han & Guan, 2007; Biswas & Stemmler, 2012; Huyer & Grant, 2012; Aleksei, 2023) developed theoretical equations to describe vortex motion and proposed various vortex models, such as Rankine vortices (Burgers, 1948) and Taylor vortices (Shtern, 2018), among others. These models have, to some extent, described the motion of vortices but often oversimplify the actual flow dynamics. Furthermore, as

Nomenclature				
ρ	density	t	time	
$\boldsymbol{u}$	velocity	k	turbulent kinetic energy	
g	gravitational acceleration	F_s	source term related to surface tension	
σ	surface tension coefficient	κ	curvature of the gas-liquid interface	
α	volume fraction (-)	θ_w	contact angle caused by the wall adhesion	
$\hat{n}$	unit normal vector at the gas-liquid interface	$\hat{n}_w$	wall unit normal vector	
$\hat{t}_w$	wall unit tangent vector	μ	viscosity	
$\tilde{P}_k$	turbulent kinetic energy generated by eddy shear	x_i	coordinate	
u_i	velocity component	ω	vorticity	
$\beta,$		v_t	eddy viscosity	
$\beta*$	turbulent coupling coefficient	μ_t	dynamic viscosity	
β_1		α_1	constant of Prandtl-Kolmogorov	
β_2		ϕ	constant that controls the conversion rate of turbulent energy	
σ_k		ϕ_1	constant that controls flow rotation and turbulent energy	
σ_{k1}		ϕ_2	constant controlling the turbulent kinetic energy dissipation rate and shear stress	
σ_{k2}	correlation constant of turbulence			
σ_ω	dissipation rate			
$\sigma_{\omega 1}$		$CD_{k\omega}$	turbulence coupling coefficient in $k-\omega$ model	
$\sigma_{\omega 2}$		ε	turbulent dissipation rate	
F_1	wall function	TX	stretching in the X direction.	
F_2	correction function	TY	stretching in the Y direction.	
TY	stretching in the Y direction.	TZ	stretching in the Z direction.	

they are all based on the Navier-Stokes equations, they lack theoretical analytical solutions.

In recent years, the advancement of Computational Fluid Dynamics (CFD) technology has furthered the study of vortices. Through simulation calculations, the flow details within a water sump can be accurately reproduced. Škerlavaj (Škerlavaj et al., 2014) used single-phase simulations to predict the vortices, successfully obtaining the gas-core length for vortices with a short gas core. However, for vortices with long cores, the length was underpredicted. The VOF method (Hirt & Nichols, 1981) is particularly effective in tracking changes at the gas-liquid interface, and is therefore widely employed in simulating vortices within the intake sump. Zi and colleagues (Zi et al., 2019, 2020) employed the Coupled Level-Set and Volume-of-Fluid (CLSVOF) method to calculate the inlet vortex flow in a horizontal pipe. They established a quasi-periodic relationship for the intake vortex bending and conducted an initial investigation of the merging mechanism of the vortex flows at the inlet. Huang and colleagues (Huang et al., 2020; Xianbei et al., 2022), utilizing the S-CLSVOF method (Albadawi et al., 2013), tracked the gas volume fraction within the intake vortex to assess the potential for its occurrence. Their research focused on the relative positions of the inlet pipe and the water sump, particularly with respect to horizontal flow information. They found that when the pipe is misaligned with the centerline of the sump, severe asymmetric flow separation occurs, which facilitates the observation of swirling vortices; however, submerged vortices are less easily detected.

Subsequently, many scholars have used model tests to study vortices. Rajendran and colleagues (Rajendran & Patel, 2000) utilized Particle Image Velocimetry (PIV) to capture the vortex patterns within the intake sump and employed dye to highlight the vortex structures, thereby obtaining pertinent flow field information. Other scholars, (Kawakita et al., 2012; Mohd Arif Zainol et al., 2015; Nazir & Sohn, 2018), observed the vortex in the intake sump through experimental methods, which provided a clearer understanding of the internal flow and the formation process of the vortex. Song (Song & Liu, 2021) measured the velocity field in the vortex region beneath the bell mouth of the intake sump using a volumetric three-component velocimetry system (V3V). They captured the spatial instantaneous three-dimensional velocity field of the floor-attached vortex region but did not extend their research to sidewall-attached vortices.

These scholars have thoroughly investigated the morphological characteristics and environmental conditions that contribute to the generation of floor-attached vortices. Nonetheless, further research is essential to explore the structural evolution and morphological details of submerged vortices more deeply. In this study, the VOF method was used to simulate vortices in an open intake sump, with the findings validated against physical model experiments. The research primarily focused on the region beneath the bell mouth, where vortices are more likely to form, aiming to investigate the evolution process and formation mechanism of these vortices.

2. GENERAL GUIDELINES

2. Equations

In this study, the primary fluid within the intake sump is in the liquid phase. The free surface of the liquid may fluctuate due to the operation of the pump, which can cause some gas to enter the pump device owing to its suction effect. Therefore, the influence of gas during the

fluid flow process must be considered. Since the flow process does not involve heat exchange, heat transfer is not considered. Thus, based on the mass conservation equation and momentum conservation equation, the VOF method is introduced to numerically simulate the flow field within the influent chamber. The specific equations are as follows:

Mass conservation equation:

$$\frac{\partial \rho}{\partial t} + \nabla \cdot (\rho \boldsymbol{u}) = 0 \tag{1}$$

Momentum conservation equation:

$$\frac{\partial}{\partial t}(\rho \boldsymbol{u}) + \nabla \cdot (\rho \boldsymbol{u}\boldsymbol{u})$$
$$= -\nabla P + \mu \nabla \cdot (\nabla \boldsymbol{u} + \nabla \boldsymbol{u}^T) + \rho g + \boldsymbol{F_s} \tag{2}$$

$$\boldsymbol{F_s} = \sigma \frac{\rho \kappa \nabla \alpha_g}{1/2\left((\rho_g + \rho_l)\right)} \tag{3}$$

$$\kappa = \nabla \cdot \hat{n} = \nabla \cdot (\hat{n}_w cos\ \theta_w + \hat{t}_w sin\ \theta_w) \tag{4}$$

Acceleration due to gravity is denoted by g(m/s^2), and the curvature of the gas-liquid interface is κ(m^{-1}). The surface tension coefficient, σ(N/m), affects the source term F_s(N/m^3), which is related to surface tension. The volume fraction of the phase is represented by α, and the contact angle caused by wall adhesion is denoted by θ_w(°). At the gas-liquid interface, the unit normal, wall unit normal, and wall unit tangent vectors are represented by $\hat{n}$, $\hat{n}_w$ and $\hat{t}_w$, respectively. The subscripts g and l denote the gas phase and liquid phase, respectively.

In two-phase flow of gas and liquid, the physical parameters are determined by the percentage of liquid and gas components in each control volume, known as the mixture density and mixture viscosity, which are given as:

$$\rho = \alpha_g \rho_g + \alpha_l \rho_l \tag{5}$$

$$\mu = \alpha_g \mu_g + \alpha_l \mu_l \tag{6}$$

The volume fraction of each phase follows the volume conservation equation:

$$\frac{\partial \alpha_i}{\partial t} + \boldsymbol{u} \cdot \nabla \alpha_i = 0 \tag{7}$$

$$\alpha_g + \alpha_l = 1 \tag{8}$$

2.2 Turbulence Model

For complex engineering problems, directly solving the governing equations or using large eddy simulation requires substantial computational resources. Therefore, the eddy viscosity turbulence model, after Reynolds time-averaging, is used. The SST $k - \omega$ model (Menter, 1996) combines features from the $k - \omega$ and $k - \varepsilon$ turbulence models. It utilizes the accurate wall function of the k-ω model for boundary layer flows and switches to the k-ε model beyond the boundary layer to conserve computational resources. This combination aims to balance stability in the near field and accuracy in the far field solution, thereby improving overall efficiency in computational fluid dynamics simulations. The complete equations are formulated as follows:

$$\frac{\partial(\rho k)}{\partial t} + \frac{\partial(\rho u_i k)}{\partial x_i} = \tilde{P}_k - \beta^* \rho k\omega + \frac{\partial}{\partial x_i}\left[(\mu + \sigma_k \mu_t)\frac{\partial k}{\partial x_i}\right] \tag{9}$$

$$\frac{\partial(\rho \omega)}{\partial t} + \frac{\partial(\rho u_i \omega)}{\partial x_i} = \alpha \frac{1}{v_t}\tilde{P}_k - \beta \rho \omega^2 + \frac{\partial}{\partial x_i}\left[(\mu + \sigma_\omega \mu_t)\frac{\partial \omega}{\partial x_i}\right] + 2(1 - F_1)\rho \sigma_{w2}\frac{1}{\omega}\frac{\partial k}{\partial x_i}\frac{\partial \omega}{\partial x_i} \tag{10}$$

The constant ϕ in this model satisfies the following relation with the constant ϕ_1 in the k-ω model and ϕ_2 in the k-ε model:

$$\phi = F_1\phi_1 + (1 - F_1)\phi_2 \tag{11}$$

The viscosity of moving eddy current is defined as:

$$v_t = \frac{a_1 k}{max(a_1\omega, SF_2)} \tag{12}$$

The closure coefficient and auxiliary relation in the model are expressed as:

$$\tilde{P}_k = min\left[\mu_t \frac{\partial u_i}{\partial x_j}\left(\frac{\partial u_i}{\partial x_j} + \frac{\partial u_j}{\partial x_i}\right), 10 \cdot \beta^* \rho k\omega\right] \tag{13}$$

$$F_1 = tanh\left\{\left\{min\left[max\left(\frac{\sqrt{k}}{\beta^*\omega y}, \frac{500v}{y^2\omega}\right), \frac{4\rho\sigma_{\omega2}k}{CD_{k\omega}y^2}\right]\right\}^4\right\} \tag{14}$$

$$F_2 = tanh\left[\left[max\left(\frac{2\sqrt{k}}{\beta^*\omega y}, \frac{500v}{y^2\omega}\right)\right]^2\right] \tag{15}$$

$$CD_{kw} = max\left(2\rho\sigma_{\omega2}\frac{1}{\omega}\frac{\partial k\partial\omega}{\partial x_i\partial x_i}, 10^{-10}\right) \tag{16}$$

$$\beta^* = 0.09, \ \alpha_1 = \frac{5}{9}, \ \beta_1 = \frac{3}{40},$$

$$\sigma_{k1} = 0.85, \ \sigma_{\omega1} = 0.5,$$

$$\alpha_2 = 0.44, \ \beta_2 = 0.0828, \ \sigma_{k2} = 1, \ \sigma_{\omega2} = 0.856$$

2.3 Boundary Conditions and Solution Methods

The inlet and outlet boundary conditions are specified as follows: hydrostatic pressure is set at the inlet, and velocity is set at the outlet. The walls are given a solid boundary condition with a no-slip condition. The upper part of the air domain is defined as an open boundary with standard atmospheric pressure. The gas inlet boundary condition is established as a velocity inlet with a zero velocity value. The volume fraction is defined according to the initial conditions: the air domain as the gas phase and the remainder as the liquid phase. Finite volume methods are employed to solve the discretized equations, and high-resolution schemes are applied to the convective terms to enhance the accuracy of the solutions.

3. EXPERIMENTS AND GEOMETRIC MODELS

3.1 Test Rig

To conduct a visual study of the vortices in the intake sump, an experimental facility was established under the support of the Research Center of Fluid Machinery Engineering and Technology in Jiangsu University. The test rig comprised a forebay, an intake sump, a vertical axial-flow pump, a torque sensor, an electromagnetic flowmeter, PVC pipes, and stainless-steel valves, as illustrated in Fig. 1. The wall of the intake sump was made of highly transparent organic glass with a thickness of 5 mm. High-definition cameras were installed on the side
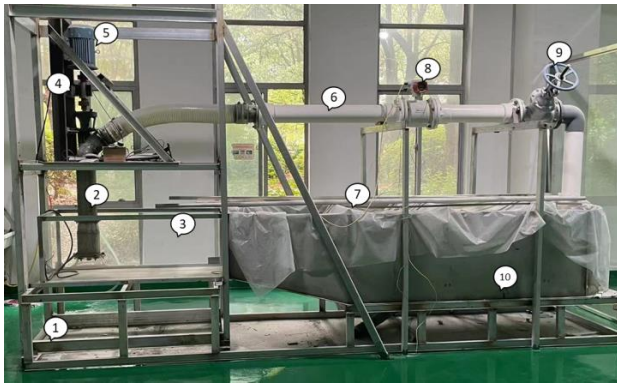
Fig. 1 Test rig

Fig. 2 Flow stability test

and rear walls to capture the vortex formation process for analysis. A rectifier was used to ensure the uniformity of the incoming flow and to reduce the effects of liquid level fluctuations on the vortices.

The specific experimental procedures were as follows:

1. Fill the channel with water to a predetermined level and remove any gas present.

2. Start the axial-flow pump with the valve fully open, allowing the water level to decrease, then readjust the water level to the predetermined value.

3. Begin the experiment once the pump has stabilized, and gradually adjust the flow from high to low in successive steps.

4. After each valve adjustment, wait for the flow to stabilize before taking measurements.

1—experimental bench bracket; 2— pump; 3—inlet sump; 4—torque measuring instrument；5—Motor;6—pipeline; 7—rectifier gate；8—electromagnetic flow meter；9—valve；

10—front reservoir.

3.2 Uncertainty Analysis

The stability of flow rates is critical in this experiment. We performed comprehensive reliability tests on the experimental system to evaluate uncertainties. Using an electronic flow meter and valves to control the flow, the meter provided an accuracy of ±1% and a resolution of 0.1m³/h.

The experiment involved taking multiple measurements at three different operating points. At consistent valve openings, we recorded data points every 10 seconds, totaling 40 measurements for each operating condition, as shown in Fig. 2. The tests, "test1," "test2," and "test3," corresponded to flow rates of 50 m³/h, 60 m³/h, and 70 m³/h, respectively.

The graphical representation showed a consistent distribution of measurement data around their respective test points. The mean and median values were within the interquartile range, with no outliers. Notably, as the flow rate increased, the interquartile range decreased, suggesting reduced variability and higher measurement
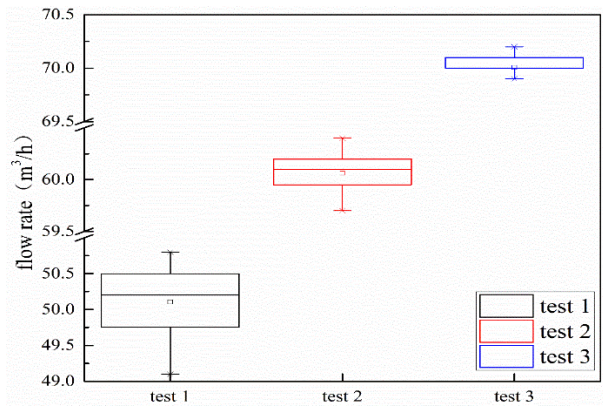
precision, especially at lower flow rates where the flow meter may have greater errors.

Calculations confirm that the maximum variation across all data remains below 1%, demonstrating that our experimental measurements conform to the accepted standards. This detailed analysis provides a comprehensive understanding of the flow meter's performance under different flow conditions.

For detailed experimental information and procedures, refer to the published paper by researchers (Hou et al., 2023).

3.3 Geometric Model

A 1:1 scale computational model was created to align with the experiments, as depicted in Fig. 3(a), with important geometric parameters indicated in Fig. 3(b). The numerical values of these physical parameters are listed in Table 1.

3.4 Grid Generation and Independence Verification

Using ICEM for grid generation, we employed a block-based approach to create a hexahedral mesh, aiming to maintain grid quality above 0.5 and to control angles within the range of 20° to 160°. Due to the complex flow characteristics near the bell mouth, we refined the grid in this vicinity. Additionally, we applied grid refinement around the blades to achieve more precise results, as shown in Fig. 4.
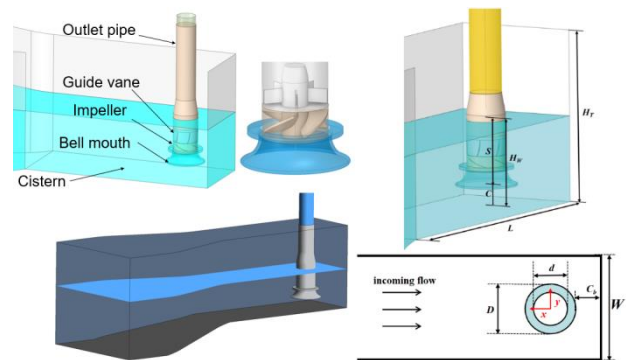
(a)three-dimensional view   (b)parameters label

Fig. 3 Diagram of the geometric model of the intake sump

Table 1 Parameters of the Intake sump geometry model

Basic parameters	Date
Inlet flare diameter D	300mm
Inner diameter of inlet pipe d	187mm
Distance between flare and bottom surface C	100mm
Width of inlet channel W	600mm
Length of inlet L	1522mm
Height of inlet H_T	850mm
Distance between inlet pipe center and rear wall C_b	300mm
Flared suction inlet submergence depth S	300mm
Water level height H_W	400mm
Impeller diameter	184mm
Impeller blades number	4
Impeller hub ratio	0.406
Guide vane blades number	6

Table 2 Grouping of grids

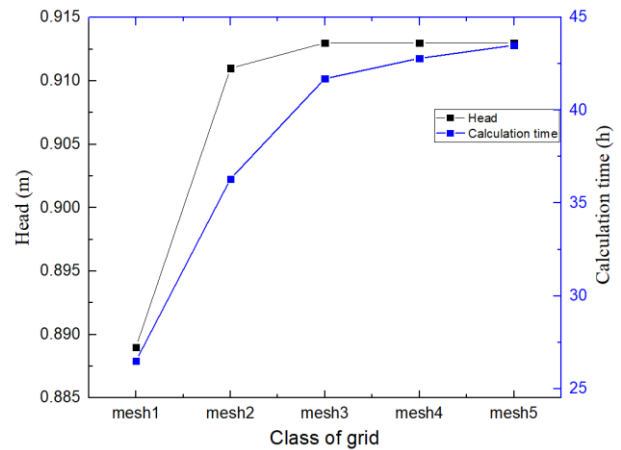| Groups of grids	Quantity
mesh1	9.2 million
mesh2	10.2 million
mesh3	11.2 million
mesh4	12.2 million
mesh5	13.2 million

Fig. 5 Variation of pump head and calculation time under different grid numbers

pump is basically stable, indicating that the number of grids has met the basic requirements at this time. The computation time increases as the number of grids increases. Therefore, to save computational resources, a grid count of 11.2 million was chosen.

4. RESULTS ANALYSIS AND DISCUSSION

4.1 Comparison of External Characteristics Of Axial Flow Pump

We have obtained the external characteristic curve of the axial-flow pump through experiments and numerical simulations at a rotational speed of 1000 rpm, as illustrated in Fig. 6.
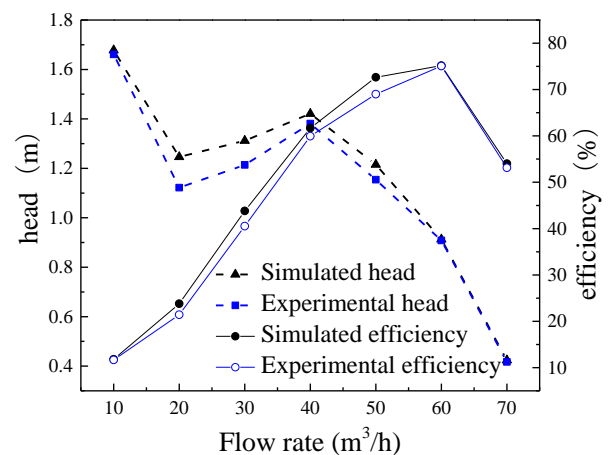

Fig. 4 computational mesh

To ensure that the number of grids meets the requirements while conserving computing resources, we generated five sets of structured grids for grid independence analysis. These grid groups are presented in Table 2.

The grid independence is analyzed by comparing the head changes under the condition that the axial flow pump speed is 1000 rpm and the design flow rate is 60m³/h. Figure 5 shows the curve of grid grouping with head change. It can be seen from the figure that when the number of grids exceeds 11.2 million, the head of the

Fig. 6 External characteristic curve

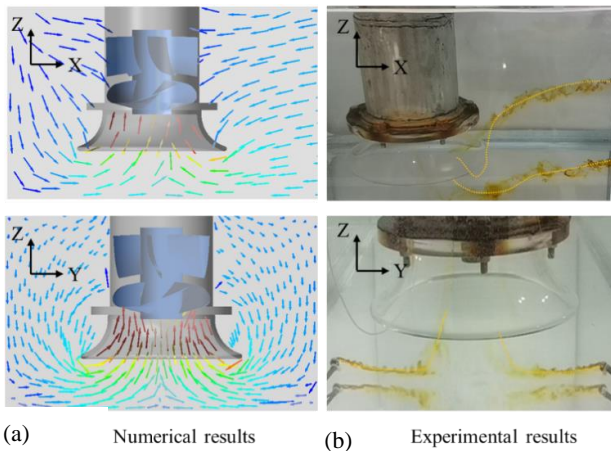(a) Numerical results   (b) Experimental results

Fig. 7 Velocity vector diagram under the condition of flow rate of 40 m3/h outside the inlet pipe. (a)Numerical results. (b)Experimental results

The numerical calculation results are consistent with the experimental data, showing good agreement with the design conditions at high flow rates. However, at low flow rates, specifically between 10 m³/h to 40 m³/h, the head curve demonstrates a distinct saddle area, where it first decreases and then increases, leading to unstable operation. This instability is due to disordered flow patterns within the pump section at low flow rates. When the flow rate exceeds 50 m³/h, the pump head exhibits a downward trend with an increased rate of decline. Previous studies indicate that an increase in flow rate intensifies liquid level fluctuations in the sump, resulting in the creation of an entrainment vortex. This vortex allows a significant amount of gas to enter the pump, adversely affecting the head and efficiency. Nevertheless, the error between the numerical calculations and experimental results falls within an acceptable range, verifying the accuracy of the method.

Moreover, Fig. 7 displays the velocity vectors around the inlet pipe at a flow rate of 40 m³/h. The velocity vectors obtained from both numerical simulation and experimental observations maintain a similar flow pattern. Numerical results indicate a gentle flow of water outside the inlet pipe and a significant velocity gradient near the bell mouth. The experimental findings corroborate this, with a noticeable dye coloration on the outer side of the intake pipe that moves smoothly with the water towards the bell mouth. Closer to the bell mouth, the dye dilutes, signaling an increase in flow velocity. These consistent results further validate the accuracy of the simulation method.

4.2 Selection of Vortex Identification Method

As seen in Fig. 8, at a flow rate of 40 m³/h, the water flow is relatively gentle, and the vortex area is relatively confined. For vortex identification, we have utilized the Q, Ω and Ω-*Liutex* criterion (Chaoqun & Yifei, 2023; Heng et al., 2023). To understand the definitions of these three methodologies, readers are referred to the scholarly works by Liu and Ehsan et al. (Duo et al., 2022; Wang et al. 2023; Bai et al. 2023; Morteza, 2023; Zheng, 2023). The Q criterion level is set at 150 s⁻², the Ω criterion threshold is 0.52, and the
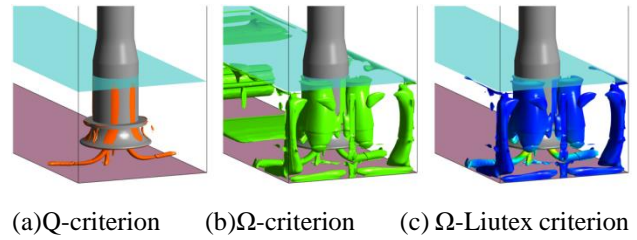

(a)Q-criterion   (b)Ω-criterion   (c) Ω-Liutex criterion

Fig. 8 Vortex morphology under different identification methods

(a)40m³/h   (b)50m³/h

(c)60m³/h   (d)70m³/h

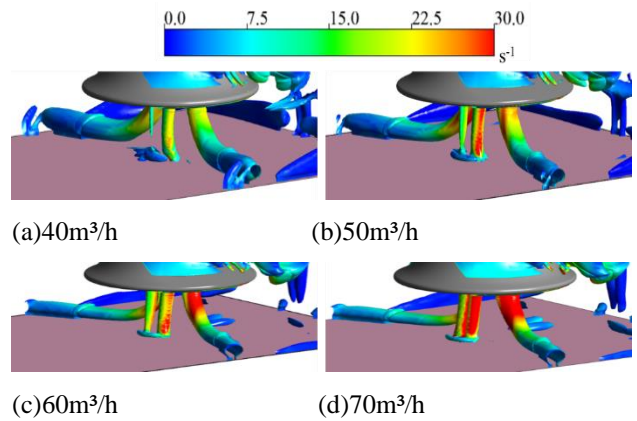**Fig. 9 Variation of vortex morphology with flow rate (The legend represents the vorticity of the rotating part based on the Liutex criterion)**

Ω-*Liutex* criterion threshold is also 0.52. From Fig. 8, we observe that the Q criterion identifies fewer vortices, while the Ω and Ω-*Liutex* criteria more comprehensively identify vortex structures, capturing them in angular regions, near-wall regions, and at the bottom of the sump. However, the Ω criterion tends to predict transitions in more distant regions. Therefore, this paper adopts the Ω-*Liutex* criteria for vortex identification to ensure result accuracy. Wang et al. (2019) provide a vector expression within the Ω-*Liutex* criteria that accurately represents the rigid rotation part of local fluid motion.

$$R = \left[\omega \cdot r - \sqrt{(\omega \cdot r)^2 - 4\lambda_{ci}^2} \right] \cdot r \qquad (17)$$

Where r represents the real eigenvector of the velocity gradient tensor (∇V), and λ_{ci} is the imaginary part of the complex conjugate eigenvalues of the velocity gradient tensor.

4.3 Analysis of Submerged Vortex Morphology

Figure 9 depicts the vorticity cloud diagram of the rotational portion of the vortex, based on the *Liutex* criterion, using isophotes. As flow increases, the submerged vortex structure grows progressively. It is apparent that floor-attached vortices begin to form a double vortex column structure at a flow rate of 40 m³/h. One vortex column structure has just formed and starts to extend towards the bottom of the sump. Increased flow further stabilizes the double vortex column structure. Near the bottom of the sump, the bases of the two vortex columns begin to merge, with the trend of integration extending throughout the vortex column and the vorticity
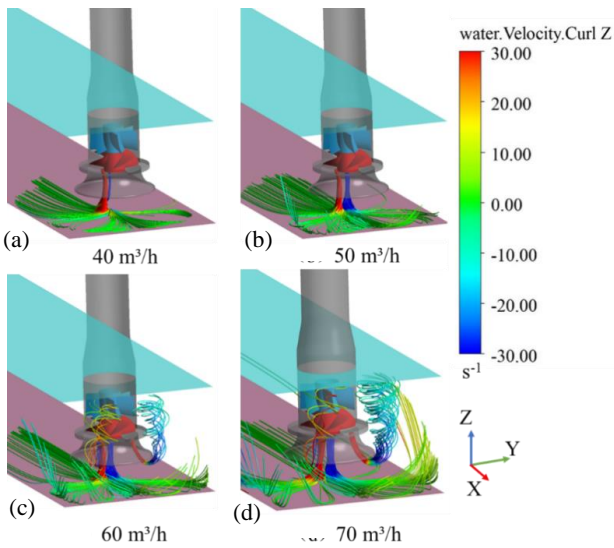
Fig. 10 Morphology of submerged vortex lines (The legend represents the component of vorticity in the Z direction)

Fig. 11 Vorticity distribution at the bottom of sump (The legend represents the component of vorticity in the Z direction)

value increasing steadily. The sidewall-attached vortices on both sides exhibit a small vortex tube radius at their attachment points and then extend along the bottom of the sump towards the bell mouth. At the lower part of the bell mouth, the impeller's suction effect alters the direction of this stretching. The vortex tube radius then becomes relatively stable and begins to increase near the flare, with the vorticity value also rising. These results suggest that the area closer to the impeller experiences stronger fluid rotation and suction actions, leading to more stable vortex columns. Additionally, a comparison between the surfaces of floor-attached and sidewall-attached vortices reveals folds on the surfaces of the sidewall-attached vortices. This is because the sidewall-attached vortices, being influenced by the sump bottom, experience disrupted structural continuity, which may lead to the surface of the vortex tube folding or even fracturing. It also indicates that the flow in this area is relatively complex, complicating vortex identification.

The vortex region has been delineated using an Iso-clip, with a specific focus on the floor-attached vortex area for streamline analysis, as illustrated in Fig. 10. In examining the streamlines, the impact of the impeller is noticeable, particularly in the region beneath the bell mouth, where heightened vorticity is observed. In this analysis, the color scheme indicates the direction of rotation: red signifies a rotation aligned with the impeller, while blue indicates a rotation in the opposite direction. Concurrently, as the streamline spreads along the bottom of the sump, the vorticity of the diffusing streamlines decreases, suggesting that the fluid's rotation weakens, which is consistent with the gentler flow in the far field. In the direction of both side walls and the rear wall area, the streamline begins to rise toward the wall as the flow rate increases. Although no high vorticity areas are present in these two directions, two vortex structures form in the rear wall area, extending to the water surface. These structures combine with the surface ripple vortices created by the liquid's surface to produce entrainment vortices,
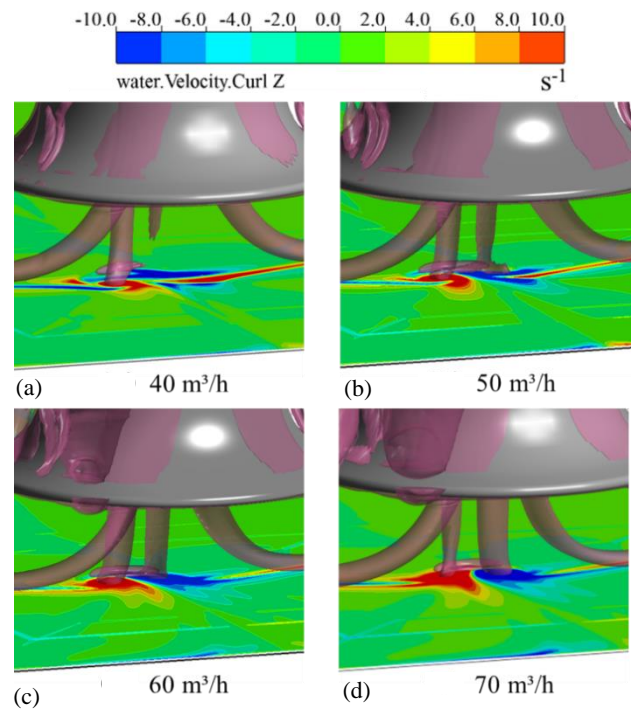
corroborating findings from previous studies (Hou et al., 2023).

Conversely, Fig. 11 illustrates the vorticity change at the position where the floor-attached vortex column meets the bottom of the sump. At low flow, one of the vortex columns has not yet fully extended to the bottom of the sump, but signs of vortex fusion are already evident at the bottom. With increasing flow, the vortex column stabilizes, and the two vortex regions with opposite rotation directions become more distinct, creating a pronounced interface between them. Due to the presence of this interface, vortices cannot merge along it; hence, they spread outwards, forming a fusion area in the outer ring. This raised ring vortex links the two vortex columns to form a U-shaped structure, as shown in Fig. 12. The connecting structure at the bottom resembles a bar-shaped vortex envelope (Xu et al., 2013; Yang, 2015; Tian, 2017) that connects the two columns, providing a channel for the exchange of matter and energy.

Figure 13 displays a velocity vector cloud image below the bell mouth. Streamlines are concentrated on the edge of the vortex tube, forming distinct boundaries. At these boundaries, incoming streams from different directions constantly collide and merge, creating velocity dead zones that significantly reduce flow efficiency and generate considerable dissipation. The turbulent dissipation frequency in Fig. 14 accurately reflects this phenomenon, with regions of high dissipation frequency concentrated along these boundaries.

The results in Fig. 15, obtained by applying the *Liutex* method to identify a wall-attached vortex structure, show that the flow pattern remains relatively unchanged with increased flow rate. The structure is symmetrical about the
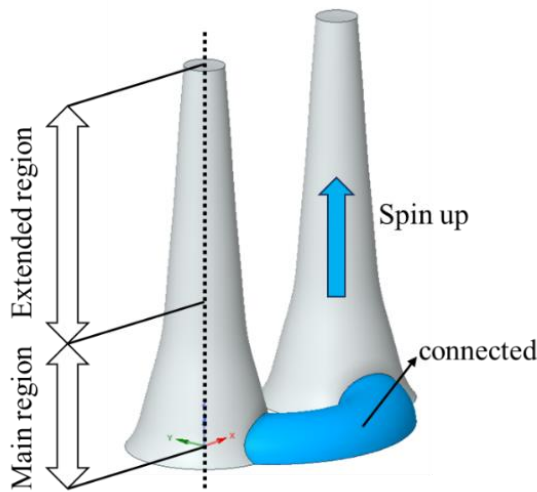
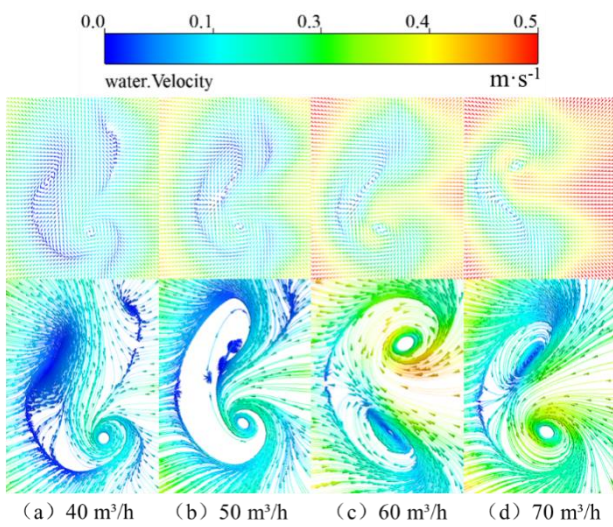Fig. 12 Floor-attached vortex of U-shaped structure
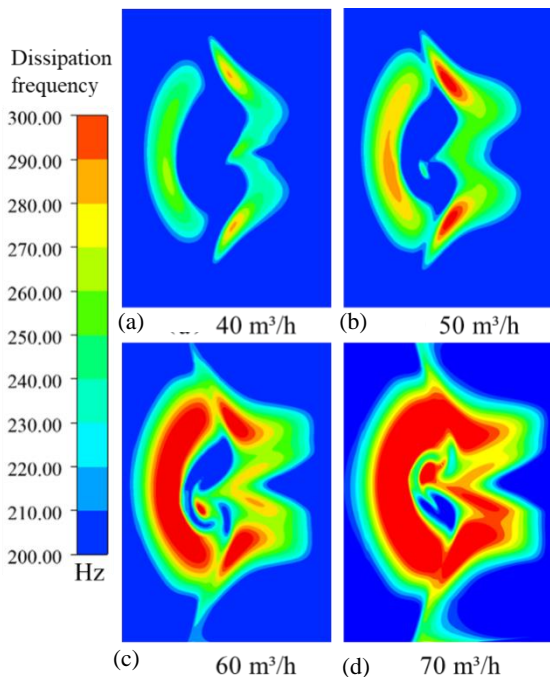

Fig. 13 Streamlines at the bottom of sump

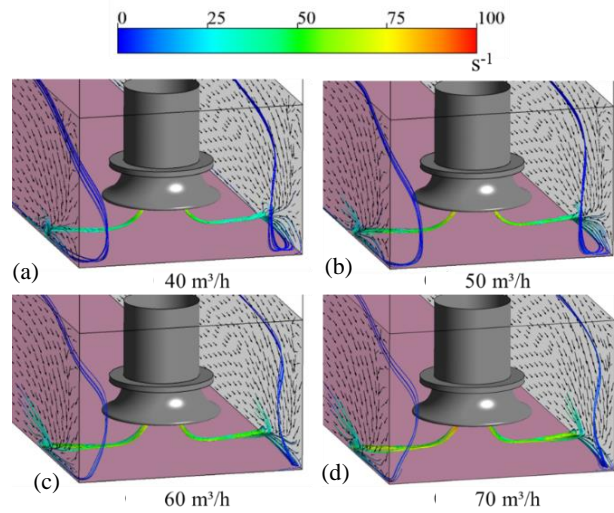Fig. 14 Dissipation frequency of floor-attached vortex

Fig. 15 The streamline of the wall-attached vortex (The legend represents the component of vorticity in the Z direction)

central axis of the sump on both sides. The double-vortex structure originates at the bell mouth and grows toward the side walls, with the growth direction perpendicular to them. In the corner area near the pool, the streamlines make a sharp turn, while near the corner area, on the sides of the wall, the velocity vectors display evident disarray.

Further analysis of the left vortex structure, as shown in Fig. 16, reveals that the incoming flow undergoes shear at the bottom of the sump, reducing the velocity of the fluid near the wall compared to the fluid above. Near the bell mouth, the impeller's suction accelerates the fluid, with the faster fluid reaching the bell mouth first and changing direction under the impeller's influence. The resulting speed differential forms a wall-attached vortex that rolls in the direction of the inlet pipe, confirming that the speed difference is the primary cause of the wall-attached vortex.
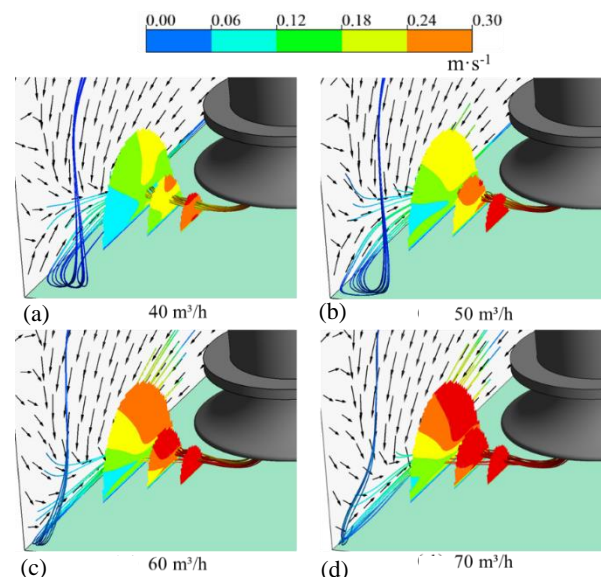
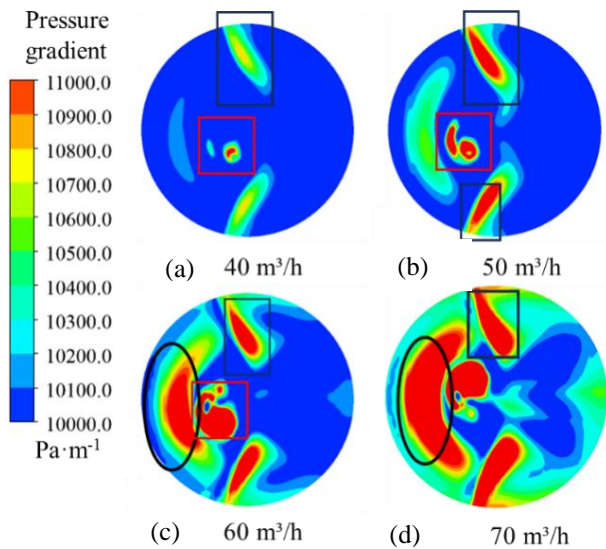

Fig. 16 Velocity distribution of wall-attached vortices

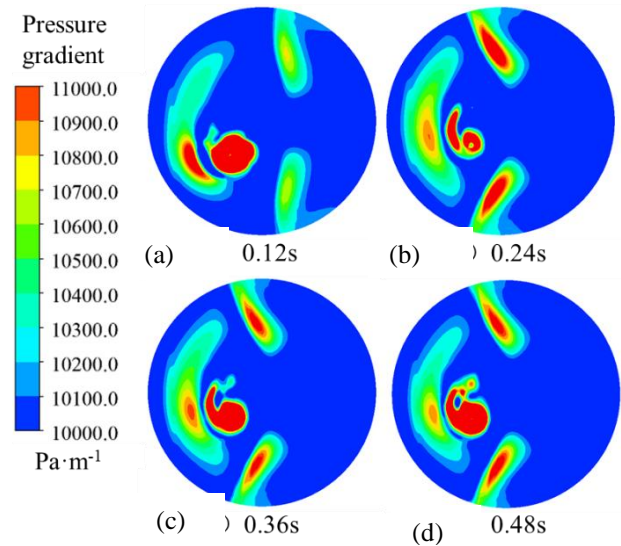**Fig. 17 Changes of pressure gradient of submerged vortex with flow rate**

Fig. 18 Pressure gradients at different times

4.4 Pressure Characteristics of Submerged Vortices

The occurrence of a vortex is greatly related to the fluid velocity gradient. Different velocities produce different pressures. The pressure within the vortex core is closely related to the surrounding pressure; therefore, the pressure gradient is introduced to analyze the pressure characteristics of the vortex, as shown in Fig. 17. The pressure gradient is defined as follows:

$$\tau_p = \frac{dP}{dr} \tag{18}$$

Where P represents the instantaneous pressure around the vortex, and r is the distance from the center of the vortex. The left side of the image shows the direction of the incoming flow, the upper and lower boundaries represent the side walls of the sump, and the right boundary is the rear wall. As the flow increases, the extent of the vortex area gradually expands. The area within the red box is the region of floor-attached vortices. At low flow, this region contains only a small vortex area, which then continuously expands with the increase of flow until it is almost circular. In the black box area, there is a wall-attached vortex region presenting a strip shape, consistent with the structure of the wall-attached vortex identified by the *Liutex* criterion. Notably, in the direction of the incoming flow—in the oval box area—there is a crescent-shaped high pressure area. This shape aligns with the edge of the bell mouth, indicating that the fluid is impeded as it flows through the bell mouth, and its velocity is converted into pressure, thus forming the crescent-shaped high pressure area in the direction of the incoming flow. Overall, the pressure distribution beneath the bell mouth is disordered, but it is roughly divided into three high-pressure regions: the central pressure region formed by the floor-attached vortex, the side pressure region formed by the wall-attached vortex, and the pressure region generated by the edge of the bell mouth.

These pressure zones not only vary with the flow rate but also with time. The operating condition of 50 m³/h is chosen, as depicted in Fig. 18. With the pump in operation,
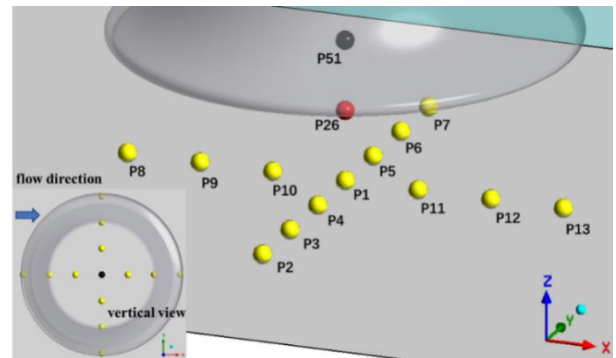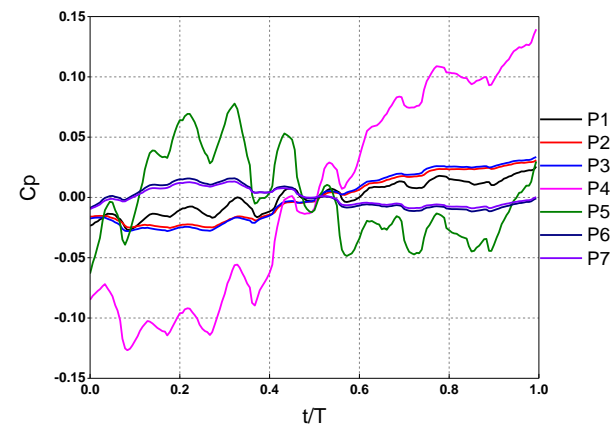

Fig. 19 Location of monitoring points

these pressure zones continue to fluctuate; the pressure level and the shape of the high-pressure zones change, which can affect the pump apparatus. Contact with these fluctuating pressures induces vibrations in the apparatus.

The area below the bell mouth is selected for further study, with monitoring points set as shown in Fig. 19. The distance between adjacent monitoring points is 50 mm. The dimensionless parameter c_p is used to describe the pressure pulsation at the monitoring points. The specific formula is as follows, where $\vec{v}$ represents the velocity at each monitoring point at the corresponding time, and $\bar{P}$ is the average pressure at the monitoring point during this period. This approach ensures that both velocity and pressure are considered simultaneously for accurate results.

$$C_p = \frac{P - \bar{P}}{0.5\rho\vec{v}^2} \tag{19}$$

As shown in Fig. 20, under a flow rate of 50 m³/h, the pressure pulsation at the monitoring point is in a very chaotic state at low flow conditions. In the Y direction, the c_p fluctuations of P4 and P5 are the most intense. These two points are located in the attachment area between the vortex and the bottom of the sump and exhibit opposite pulsation phenomena. The fluctuations of P6 and P7 on the same side and P2 and P3 on the opposite side also display
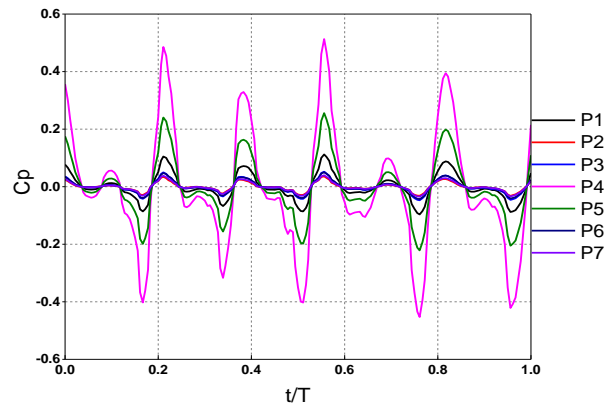
(a)Pressure pulsation at monitoring points in Y direction
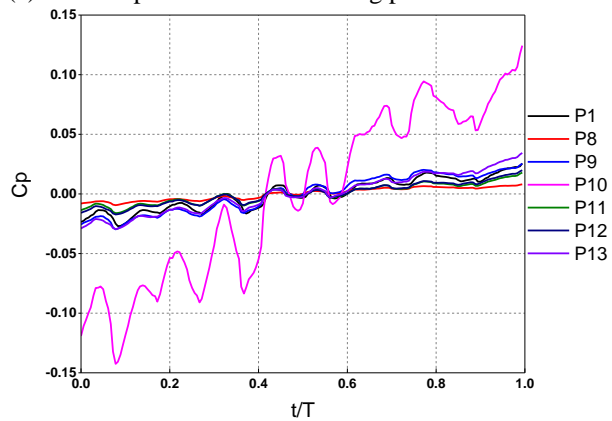
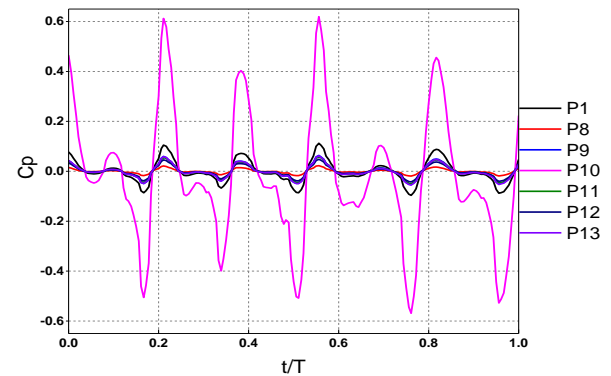

(b)Pressure pulsation at monitoring points in X direction
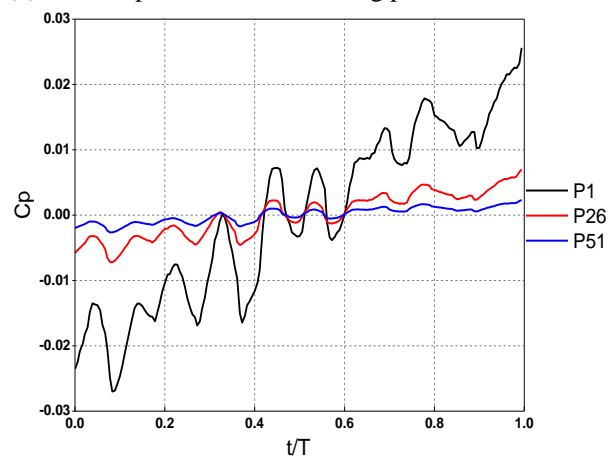
(c)Pressure pulsation at monitoring points in Y direction

Fig. 20 Pressure fluctuation of monitoring points under the flow rate of 50 m3/h (X, Y, and Z correspond to the three directions shown in Fig. 19)

(a)Pressure pulsation at monitoring points in Y direction

(b)Pressure pulsation at monitoring points in X direction

(c)Pressure pulsation at monitoring points in Y direction

Fig. 21 Pressure fluctuation of monitoring points under the flow rate of 70 m3/h (X, Y, and Z correspond to the three directions shown in Fig.19)
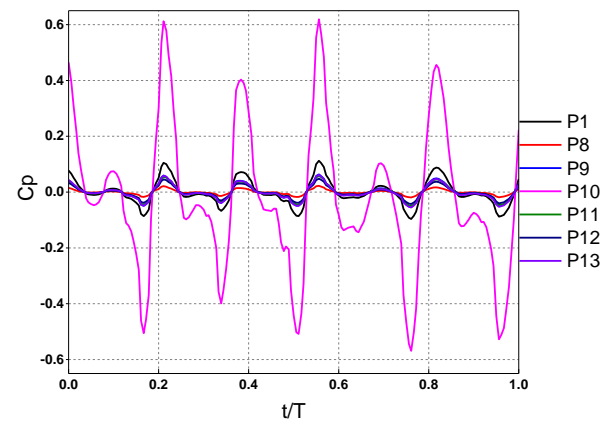
the same pattern, which is related to the rotation direction of the vortex. In the X direction, c_p shows a slow increasing trend. The pulsation amplitude at P10 is much higher than that of the other monitoring points in the same direction, with eight irregular pulsation periods. This point is situated in the pressure zone generated by the edge of the bell mouth. Under low flow conditions, the flow state itself is unstable, and the presence of submerged vortices exacerbates the pressure pulsation at that location. In the Z direction, the overall pulsation amplitude is smaller than in the other two directions. The monitoring point on the

axis, the closer to the shaft, the smaller the pulsation amplitude, indicating that the submerged vortex is significantly sheared by the bottom of the sump, and the pressure fluctuation is more pronounced near the wall.

On the other hand, under a large flow rate condition, which is 70 m³/h, the pressure pulsation shows significant periodicity, and the peak value is higher than that at low flow rates, as shown in Fig. 21.

The maximum peak in the X direction is higher than in the other directions, and the pressure pulsation in each direction reveals six pulsation periods. At a large flow rate, the vortex structure is relatively stable. Compared with the low flow rate condition, the flow trajectory is more stable, resulting in relatively stable pressure pulsations, with two
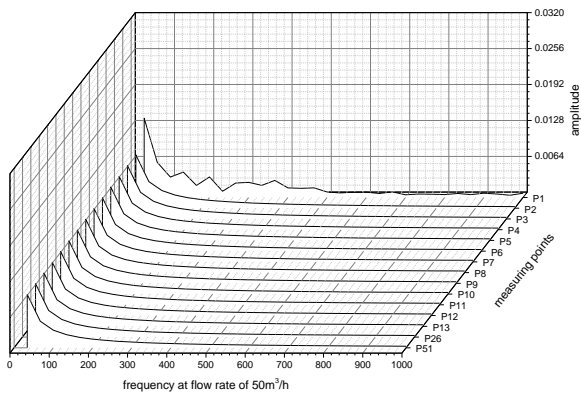
(a) frequency at flow rate of 50m^3/h
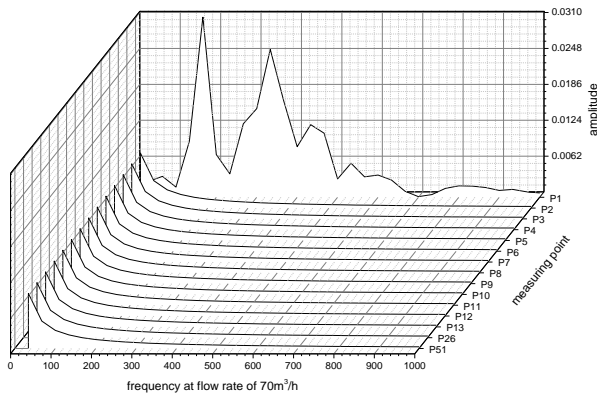
(b)frequency at flow rate of 70m^3/h

Fig. 22 Frequency domain distribution under different flow rates

of the six pulsation periods having smaller amplitudes. Normally, the pressure pulsation frequency near the impeller is equivalent to the blade frequency. When the impeller completes one rotation, four pulsation periods are generated. The two additional small pulsations correspond to the two floor-attached vortices. Furthermore, the curve with the largest fluctuation amplitude in the figure corresponds to points P4 and P10, which are also near the position of the floor-attached vortex.

It can be seen from Fig. 22 that the amplitude of the pressure pulsation is primarily concentrated in the low-frequency band. With the exception of the P1 measuring point, the amplitude curves of the other points align, indicating that they share the same periodic characteristics. The only difference is the amplitude under a small flow condition is smaller than under a large flow condition. The corresponding dominant frequency is concentrated near the shaft frequency. Since the P1 measuring point is directly below the main shaft, which corresponds exactly to the merging point of the double vortex column structure, there is a strong vortex pulsation, and the frequency increases with the flow rate.

4.5 Structural Evolution of Floor-Attached Vortices

During the experiment, dye was introduced directly below the bell mouth at a constant and stable rate to visualize the trajectory of the vortex. The results, depicted in Fig. 23, show a flow rate of 60 m³/h. On a temporal
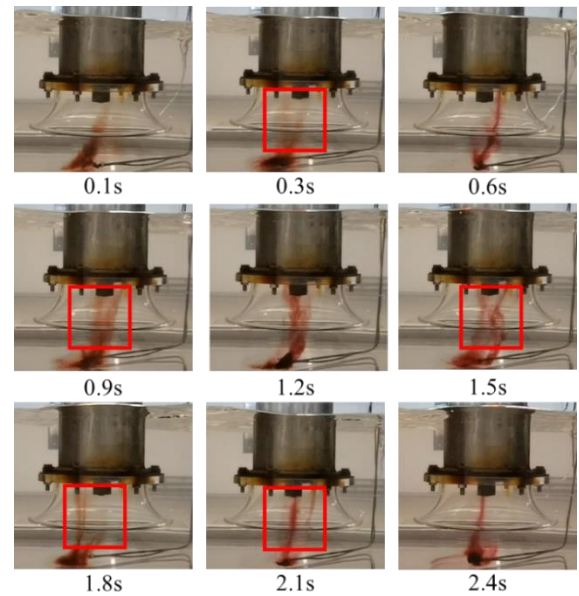

Fig. 23 Dyeing results with floor-attached vortex

scale, the double vortex structure does not persist continuously; the floor-attached vortex alternates between single and double vortex structures. The red box in the figure highlights the double vortex structure. In terms of dye concentration, the color of the single vortex is darker, and it becomes lighter when transitioning into a double vortex structure. However, at the bottom of the sump, the dye accumulates, maintaining a high concentration and a darker color. This is in line with the previously described U-shaped structure of the floor-attached vortex. The vortex package at the bottom traps most of the dye within it.

The transformation between vortex structures inevitably involves changes in velocity and vorticity, so helicity (Scheeler et al., 2014; Baj et al., 2022) is employed for analysis. The formula is given as follows:

$$H_d = \boldsymbol{\mu} \cdot \boldsymbol{\omega} \tag{20}$$

$$H_n = \frac{\boldsymbol{\mu} \cdot \boldsymbol{\omega}}{|\boldsymbol{\mu}| \cdot |\boldsymbol{\omega}|} \tag{21}$$

Where $\boldsymbol{\mu}$ represents velocity, $\boldsymbol{\omega}$ represents vorticity, and H_n is the normalized result of helicity H_d. Figure 24 tracks the helicity variation at the bottom section of the sump directly below the bell mouth over time. At the initial formation of the floor-attached vortex, two primary vortices with opposite rotation directions appear on the cross-section. Near the primary vortices, within the area marked by the black box, there are two small-scale vortices with opposite rotation directions. These small-scale vortices, situated within the vicinity of the two large-scale vortices, are encapsulated by the vortex packet, revealing a complex small-scale vortex system within the vortex. At 0.18s, the small-scale vortices absorb energy from the main vortices, leading to their development and the decay of the large-scale vortices, resulting in a typical quadrupole vortex structure with alternately rotating vortices. At 0.24s, within the red square, a new pair of vortices forms on the right side of the original main vortices. The small-scale vortices siphon energy from the
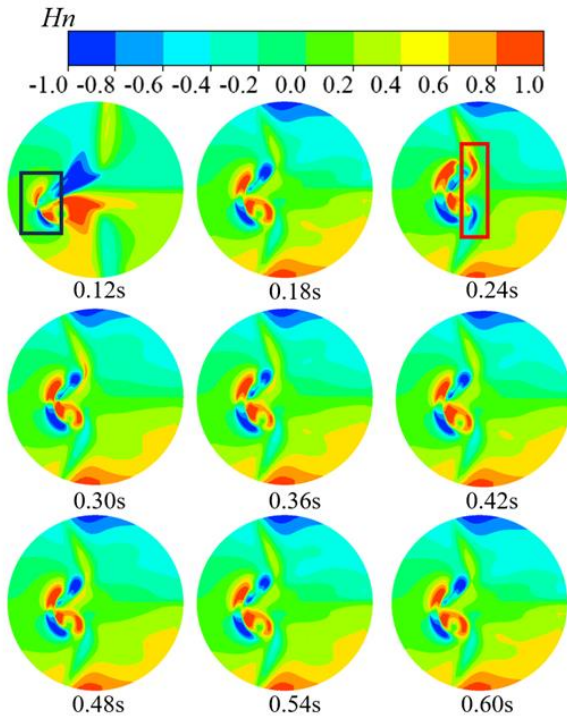
Fig. 24 The change of H_n with time

(a)　　　　　(b)　　　　　(c)

Fig. 25 Cloud images of *TX*, *TY* and *TZ*

larger vortices, which are referred to as the large new vortices, and are then segmented by the surrounding small vortices. The interchange of vortex scales signifies the exchange of vorticity and velocity, culminating in a stable quadrupole structure. One pair of vortices with opposite rotation is affixed to the vortex packet at the sump's bottom, while the other pair ascends, forming the vortex column structure.

To further investigate the vertical growth of the vortex, the vertical component (Ge et al., 2013) of the quasi-vortex energy transport equation is utilized for analysis. It is expressed as follows:

$$\frac{\partial\left(\frac{1}{2}\omega_z\omega_z\right)}{\partial t} = \omega_x\omega_z\frac{\partial w}{\partial x} + \omega_y\omega_z\frac{\partial w}{\partial y} + \omega_z\omega_z\frac{\partial w}{\partial z} - \omega_z\frac{\partial w}{\partial z}\frac{\partial V}{\partial y} + \omega_z v\frac{\partial^2 V}{\partial y^2} - \frac{\partial}{\partial y}\left(\frac{1}{2}v\omega_z\omega_z\right) + \frac{1}{2}\frac{\partial}{\partial y}\left[v\frac{\partial(\omega_z\omega_z)}{\partial y}\right] - v\frac{\partial \omega_z}{\partial x_j}\frac{\partial \omega_z}{\partial x_j}$$

(22)

Where $v \; and \; w$ are the mean flow velocities in the Y and Z directions, respectively, and V is the mean flow velocity within the pool. The first five terms on the equation's right side are the production terms, the sixth term represents turbulent diffusion, the seventh term is viscous diffusion, and the last term denotes dissipation. To simplify the analysis, high-order minor quantities in the equation are omitted, yielding the following simplified expression:

$$\frac{D\left(\frac{1}{2}\omega_z\omega_z\right)}{Dt} = \omega_x\omega_z\frac{\partial w}{\partial x} + \omega_y\omega_z\frac{\partial w}{\partial y} + \omega_z\omega_z\frac{\partial w}{\partial z} \; (23)$$

The three terms on the equation's right side represent the effects of $\frac{\partial w}{\partial x}$, $\frac{\partial w}{\partial y}$ and $\frac{\partial w}{\partial z}$ changes on the stretching of ω_x, ω_y and ω_z, respectively. These are denoted by *TX*, *TY*, and *TZ*. Figure 25 captures the cloud images of *TX*,
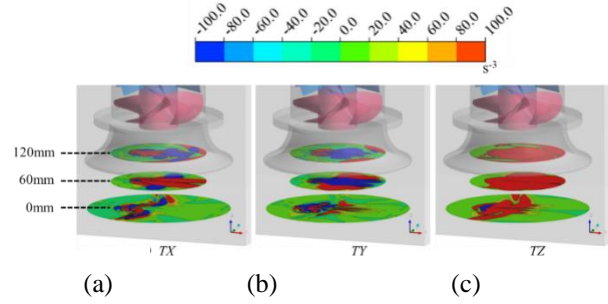
TY, and *TZ* at three different heights below the bell mouth at 0.54s.

TX and *TY* show positive and negative alternation in the graph. The closer to the bottom, the more obvious the alternation is. On the cross section of 0mm, *TX* and *TY* show a strong positive and negative alternation law, which indicates that the vortex is not stretched in these two directions but forms a complex vorticity transport system. Each positive and negative conversion is a vorticity transport process, which is consistent with the situation described above. When it is close to the impeller, the number of positive and negative alternations decreases, the path of vorticity transport decreases, and the vortex structure becomes single, from a complex quadrupole structure to a double vortex column structure. On the other hand, *TZ* displays a strong dominance on the cross section. In the Z direction, the stretching effect of $\frac{\partial w}{\partial z}$ on ω_z is significant. The vorticity transports from the bottom to the top, and the vortex grows from the bottom to the top, finally forming the structure shown in Figure 11. Accordingly, it can be considered that in the process of the formation of the floor-attached vortex, the alternating transport process of vorticity mainly occurs in the X and Y directions, which provides a complex vorticity basis for the upward growth of the vortex, and the Z direction is the stretching process of the vortex.

5. CONCLUSION

In this paper, a systematic analysis of the shape and evolution process of submerged vortices within an intake sump is conducted through a combination of numerical simulation and experimentation. Attention is given to the shape and pressure fluctuation characteristics of the vortex at varying flow rates and at different times. The following conclusions have been drawn:

(1) The size of the submerged vortex increases with the flow rate. The floor-attached vortex forms below the bell mouth and exhibits a U-shaped, double-columnar structure. At the base of this U-shaped structure lies a complex small-scale vortex system within the vortex packet, culminating in a quadrupole shape at the sump's bottom.

(2) A strip structure exists between the bell mouth of the wall-attached vortex and the sidewall of the inlet pool. One end adheres to the wall surface, while the other terminates at the impeller. The original horizontal vortex column below the impeller is drawn upwards by the

impeller, altering its direction. The formation of the wall-attached vortex is attributed to fluid experiencing variable flow rates; the fluid near the bell mouth is slowed by the pool's bottom, which shears the bottom fluid, causing it to be slower than the fluid above and thus initiating a wall-attached vortex. Consequently, incorporating hydraulic structures to manage flow velocity in subsequent inlet tank designs could effectively reduce wall-attached vortices.

(3) Below the bell mouth, the high-pressure area is primarily segmented into three regions: the central pressure area created by the floor-attached vortex, the lateral pressure area formed by the wall-attached vortex, and the pressure area arising from the edge of the bell mouth. The pressure level and boundaries of the high-pressure area exhibit pulsation, with corresponding pressure fluctuations having small amplitude oscillations related to the presence of the vortices. The confined space beneath the bell mouth and the significant pressure gradient changes promote the floor-attached vortices. Elevating the pump apparatus increases the space below, moderates the pressure gradient change, suppresses the vortex formation, and enhances the operational efficiency of the pumping system.

(4) Analysis of the vorticity transport equation reveals that at the base of the bell mouth, the closer to the pool's bottom, the vorticity transport and complexity of the vortex are influenced by the vorticity transfer from $\frac{\partial w}{\partial x}$ to ω_x and from $\frac{\partial w}{\partial y}$ to ω_y. Near the impeller, the vorticity transport path is more straightforward, and the stretching effect of $\frac{\partial w}{\partial z}$ on ω_z is predominant, playing a key role in the growth of the vortex attached to the bottom.

In conclusion, the experimental and numerical results corroborate the characteristics of submerged vortices. Therefore, this study can provide a valuable reference for related research on submerged vortices.

ACKNOWLEDGEMENTS

CONFLICT OF INTEREST

The authors have no competing interests or conflicts to disclose.

AUTHORS CONTRIBUTION

Xueliang Hou and **Jianping Yuan:** Conceptualization; methodology; formal analysis; writing original draft. **Yanxia Fu，Peng Wang，Peiyi Zhang，Naihu He:** writing review and editing. All authors have read and agreed to the published version of the manuscript.

REFERENCES

Albadawi, A., Donoghue, D., Robinson, A., Murray, D., & Delauré, Y. (2013). Influence of surface tension implementation in volume of fluid and coupled volume of fluid with level set methods for bubble growth and detachment. *International Journal of Multiphase Flow, 53*, 11-28. https://doi.org/10.1016/j.ijmultiphaseflow.2013.01.005

Aleksei, G. (2023). No-Slip boundary condition for vorticity equation in 2D Exterior domain. *Journal of Mathematical Fluid Mechanics, 25*(3). https://doi.org/10.1007/s00021-023-00795-7

Bai, T., Cheng, C., & Fu, L. (2023). Effects of mean shear on the vortex identification and the orientation statistics. *Theoretical and Applied Mechanics Letters, 13*(4). https://doi.org/10.1016/j.taml.2023.100454

Baj, P., Portela, F. A., & Carter, D. W. (2022). On the simultaneous cascades of energy, helicity, and enstrophy in incompressible homogeneous turbulence. *Journal of Fluid Mechanics, 952*(420). https://doi.org/10.1017/jfm.2022.912

Biswas, I., & Stemmler, M. (2012). Vortex equation and reflexive sheaves. *Advances in Theoretical and Mathematical Physics, 16*(2). https://doi.org/10.4310/ATMP.2012.v16.n2.a8

Burgers, J. M. (1948). A mathematical model illustrating the theory of turbulence. *Advances in applied mechanics, 1*, 171-199. https://doi.org/10.1016/j.na.2021.112277

Chaoqun, L., & Yifei, Y. (2023). Mathematical foundation of Liutex theory. *Journal of Hydrodynamics, 34*(6). https://doi.org/10.1007/s42241-023-0091-2

Duo, W. A. N. G., Chaoqun, L. I. U., Xiaoshu, C. A. I., & Hongyi, X. U. (2022). Tackling Vortex/turbulence challenges based on direct numerical simulation data in fluid science. *Chinese Quarterly of Mechanics, 43*(02), 197-216. https://doi.org/10.15959/j.cnki.0254-0053.2022.02.001

Ge, M. W., Xu, C. X., Huang, W. X., & Cui, G. X. (2013). Transient response of enstrophy transport to opposition control in turbulent channel flow. *Applied Mathematics and Mechanics, 34*(2), 127-138. https://doi.org/10.1007/s10483-013-1658-x

Han, F., & Guan, K. (2007). Qualitative analysis about infinitely many vortex flow of euler equation. *Journal of Beijing Jiaotong University*(06), 108-111.

Heng, L., Yang, L., Duo, W., & Hongyi, X. (2023). Liutex (vortex) core and tube identification and automatic generation algorithms. *Computers and Fluids, 250*. https://doi.org/10.1016/j.compfluid.2022.105731

Hirt, C. W., & Nichols, B. D. (1981). Volume of fluid (VOF) method for the dynamics of free boundaries. *Journal of computational physics, 39*(1), 201-225. https://doi.org/10.1016/0021-9991(81)90145-5

Hou, X., Yuan, J., Fu, Y., Lu, R., Shi, J., & Zhang, P. (2023). A study on the dynamic characteristics of surface suction vortices in an open inlet pool. *Physics of Fluids, 35*(6). https://doi.org/10.1063/5.0146645

Huang, X., Guo, Q., Qiu, B., & Feng, X. (2020). Prediction of air-entrained vortex in pump sump: influence of turbulence models and interface-tracking methods. *Journal of Hydraulic Engineering, 146*(4), 04020010. https://doi.org/10.1061/(ASCE)HY.1943-7900.0001708

Huang, Y., & Hu, X. (2000). Superposition of three-dimensional vortex solutions of hydrodynamic equations. *Applied Mathmatics and Mechanics* (12), 1227-1237. https://link.springer.com/article/10.1007/BF02459214

Huyer, S. A., & Grant, J. R. (2012). Solution of two-dimensional vorticity equation on a lagrangian mesh. *AIAA Journal, 38*(5). https://doi.org/10.2514/2.1057

Kawakita, K., Matsui, J., & Isoda, H. (2012). *Experimental study on the similarity of flow in pump sump models.* IOP Conference Series: Earth and Environmental Science. https://doi.org/10.1088/1755-1315/15/6/062047

Menter, F. (1996). A comparison of some recent eddy-viscosity turbulence models. *Journal of Fluids Engineering, 118*(3). https://doi.org/10.1115/1.2817788

Mohd Arif Zainol, M. R. R., Khairy, A., Abustan, I., & Al Bakri Abdullah, M. M. (2015). Model study for upgrading of Sungai Belibis pump sump. *Applied Mechanics and Materials, 802*, 617-622. https://doi.org/10.4028/www.scientific.net/AMM.802.617

Morteza, D. E. B. (2023). Analysis of the vortical flow in a cyclone using four vortex identification methods. *Powder Technology, 428*. https://doi.org/10.1016/j.powtec.2023.118897

Nazir, K., & Sohn, C. H. (2018). Effect of water temperature on air-core generation and disappearance during draining. *Journal of Mechanical Science and Technology, 32*, 703-708.

Rajendran, V. P. (1998). Experiments on flow in a model water-pump intake sump to validate a numerical model. *Proceedings of FEDSM'98, FEDSM98-5098, June 21-25, 1998, Washinton, DC*. https://cir.nii.ac.jp/crid/1573105974909273600

Rajendran, V., & Patel, V. (2000). Measurement of vortices in model pump-intake bay by PIV. *Journal of Hydraulic Engineering, 126*(5), 322-334. https://doi.org/10.1061/(ASCE)0733-9429(2000)126:5(322)

Shtern, V. (2018). *Cellular Flows: topological metamorphoses in fluid mechanics*. Cambridge University Press.

Škerlavaj, A., Škerget, L., Ravnik, J., & Lipej, A. (2014, 2014/01/01). Predicting Free-surface vortices with single-phase simulations. *Engineering Applications of Computational Fluid Mechanics, 8*(2), 193-210. https://doi.org/10.1080/19942060.2014.11015507

Song, X., & Liu, C. (2020). Experimental investigation of floor-attached vortex effects on the pressure pulsation at the bottom of the axial flow pump sump. *Renewable Energy, 145*, 2327-2336. https://doi.org/10.1016/j.renene.2019.07.125

Song, X., & Liu, C. (2021). Experimental study of the floor-attached vortices in pump sump using V3V. *Renewable Energy, 164*, 752-766. https://doi.org/10.1016/j.renene.2020.09.088

Tian, H. (2017). *PIV experimental research of coherent structures in wall-bounded turbulent flow and drag reduction mechanism by superhydrophobic surfaces* [PhD, Tianjin university].

Scheeler, M. W., Kleckner, D., Proment, D., Kindlmann, G. L., & Irvine, W. T. (2014). Helicity conservation by flow across scales in reconnecting vortex links and knots. *Proceedings of the National Academy of Sciences of the United States of America, 111*(43). https://doi.org/10.1073/pnas.1407232111

Wang, D. D., Wang, Z. H., Fan, Y. W., Sun, X., & Gao, Q. J. (2023). Characterization of vortex structures with self-excited oscillations based on Liutex-Omega vortex identification method. *Journal of Hydrodynamics, 35*(1), 95-111. https://doi.org/10.1007/s42241-023-0011-5

Wang, Y. Q., Gao, Y. S., Liu, J. M., & Liu, C. (2019). Explicit formula for the Liutex vector and physical meaning of vorticity based on the Liutex-Shear decomposition. *Journal of Hydrodynamics, 31*, 464-474.

Wu, J. (1985). Exact vortex solution of N-S equation. *Acta Aerodynamica Sinica, 1*, 80-84. https://doi.org/10.1143/JPSJ.53.13.

Xianbei, H., Qiang, G., Tao, F., Xurui, C., & Baoyun, Q. (2022). Air-entrainment in hydraulic intakes with a vertical pipe: The mechanism and influence of pipe offset. *International Journal of Multiphase Flow, 146*, 103866. https://doi.org/10.1016/j.ijmultiphaseflow.2021.103866

Xu, C., Deng, B., Huang, W., & Cui, G. (2013). Coherent structures in wall turbulence and mechanism for drag reduction control. *Science China Physics, Mechanics and Astronomy, 56*(6). https://doi.org/10.1007/s11433-013-5087-4

Yang, S. (2015). *Particle Image velocimetry investigation of coherent structures in wall-bounded turbulent flows and their passive control by riblets* [PhD, Tianjin university]. https://doi.org/10.1115/1.4038091

Zheng, L. Y. X. (2023). Application of vortex identification methods in vertical slit fishways. *Water, 15*(11). https://doi.org/10.3390/w15112053

Zi, D., Shen, L., Xuan, A., & Wang, F. (2019). *LES analyses of the air-core vortex in intake flow field of pumping station.* IOP Conference Series: Earth and Environmental Science. https://doi.org/10.1088/1755-1315/240/3/032037

Zi, D., Xuan, A., Wang, F., & Shen, L. (2020). Numerical study of mechanisms of air-core vortex evolution in an intake flow. *International Journal of Heat and Fluid Flow, 81*, 108517. https://doi.org/10.1016/j.ijheatfluidflow.2019.108517